

Short-Distance Structure of the Deuteron and Reaction Dynamics in ${}^2\text{H}(e, e'p)n$ (An Update to Experiment E94-004)

P.E. Ulmer^{†,*}, C.E. Hyde-Wright, H. Ibrahim, A. Klein, S. Kuhn, L.B. Weinstein
Old Dominion University

M. Jones[†]
The University of Maryland

J. Mitchell[†], K. de Jager, R. Ent, S. Jeschonnek, J. LeRose, A. Saha
Jefferson Laboratory

M. Epstein
The California State University at Los Angeles

J.M. Finn, C. Perdrisat
The College of William and Mary

P.E.C. Markowitz
Florida International University

K. McCormick
Kent State University

W. Bertozzi, S. Gilad, D.W. Higinbotham, S. Sirca, R. Suleiman, Z. Zhou
Massachusetts Institute of Technology

V. Punjabi
Norfolk State University

J. Adam
Nuclear Physics Institute, Rez n. Prague, Czech Republic

F. Benmokhtar, S. Dieterich, R. Gilman, X. Jiang, R.D. Ransome, S. Strauch
Rutgers University

A. Sarty
St. Mary's University

Z. Papandreou
The University of Regina

[†] Co-spokesperson

* Contact Person

Abstract

We propose a systematic study of the ${}^2\text{H}(e, e'p)n$ reaction over a large region of the kinematic phase space. In parallel and anti-parallel kinematics, a measurement of the cross section will be made for fixed Q^2 over a large range of energy transfers extending from below to above the quasifree peak. Here the focus is on the deuteron short-range structure, as FSI are expected to be minimized for these kinematics. In perpendicular kinematics on the quasifree peak, an extraction of R_{LT} will be done at three values of Q^2 . This response function is expected to be sensitive to relativistic effects. These measurements will not only constrain models of the deuteron structure and reaction mechanisms but will also provide vital input for heavier nuclei. The JLab/Hall A combination are uniquely suited to such a study.

Hall	Description	Beam Days	Energy	Max. Current
A	${}^2\text{H}(e, e'p)n$	19	4.0 GeV	100 μA

Contents

1	Overview of Goals	4
2	Relation to and Status of Previous Proposal	4
3	Relation to other JLAB Experiments	5
4	Kinematic Definitions and Formalism	5
5	Physics Motivation	7
5.1	Importance of the Deuteron	7
5.2	Overview of Existing Data on $^2\text{H}(e, e'p)n$	8
5.3	Motivation for Parallel/Anti-Parallel Kinematics	9
5.4	Motivation for Perpendicular Kinematics	11
6	Kinematics	11
7	Experimental Equipment	12
8	Single-Arm Rates	26
9	Coincidence Rates	26
10	Systematic and Statistical Uncertainties	31
11	Beam Time Summary	31
12	Acknowledgment	32

1 Overview of Goals

This experiment will study the ${}^2\text{H}(e, e'p)n$ reaction over a broad range in kinematical phase space. There are essentially two kinematical cuts (the various kinematic quantities will be defined later):

- For parallel/anti-parallel kinematics (*i.e.* protons detected along the \vec{q} vector), a measurement of the cross section will be made spanning a large range of x both above and below the quasifree peak. This measurement will be done at fixed beam energy and electron scattering angle, varying the electron final energy, proton angle and proton momentum. The kinematics at the $x = 1$ point will coincide with the middle Q^2 value for the perpendicular kinematics measurement (see below). For parallel/anti-parallel (as opposed to perpendicular) kinematics, the effects of Final State Interactions (FSI) are expected to be minimized, this allowing a clean extraction of the deuteron short-range structure. Obtaining this information is crucial not only for understanding the deuteron, but also as input on the NN interaction dynamics in more complex nuclei.
- For perpendicular kinematics on the quasifree peak ($x = 1$), a measurement of the cross section for protons on each side of the \vec{q} vector will be made to separate the interference response function, R_{LT} . This will be done at three values of Q^2 . This response function is expected to be sensitive to relativistic effects which should become more important at higher Q^2 and/or p_r . As the deuteron is the simplest “non-trivial” nucleus, it is the starting point for addressing such questions. Information garnered from this study will serve as valuable input to relativistic calculations for heavier systems.

2 Relation to and Status of Previous Proposal

The current proposal is based on and supercedes Hall A Experiment E94-004 which is now under Jeopardy. There are three main differences to that proposal:

- The current proposal does not involve separation of R_L and R_T , but only R_{LT} . Extraction of the former requires multiple beam energies and electron angles and, given the rapid variation of the deuteron momentum distribution, requires a high degree of control of systematics. The current proposal is less technically challenging.
- The current proposal will extract R_{LT} for three Q^2 values instead of two, spanning a larger range of Q^2 and p_r .
- The current proposal includes a measurement of the cross section in parallel/anti-parallel kinematics over a large range of x , whereas the kinematics of E94-004 were strictly quasielastic.

Experiment E94-004 was approved for 29 days with a B rating. In October of 1999, that experiment received 3 calendar days of running for a preliminary measurement of the cross section in perpendicular kinematics at $Q^2 = 0.66$ (GeV/c)² out to a recoil momentum of 550 MeV/c. Measurements were made on only one side of \vec{q} , so R_{LT} could

not be separated. The results of the analysis (carried out by P. Ulmer, one of the co-spokespersons of this proposal) are shown in Figure 1. The agreement between the data and the calculation of H. Arenhövel [1] is quite good. It can be seen that FSI effects are quite large at the higher recoil momenta. More will be said of this in connection with the current proposal.

Although E94-004, in its entirety, is quite technically challenging, this preliminary October run, which involved no R_L/R_T separations, had very similar technical requirements and running conditions as the current proposal. **The collaboration involved in the current proposal has thus proven itself capable of carrying out and analyzing this experiment.**

3 Relation to other JLAB Experiments

This experiment is somewhat related to the ${}^2\text{H}(e, e'p)$ Hall B experiment [2] which also studies the high momentum structure of the deuteron. The kinematic coverage of that experiment is naturally much broader than our proposal due to the large acceptance of the CLAS. It extends from the elastic channel (*i.e.* np final state) through the resonance and into the deep inelastic region, covering a broad range of Q^2 and out-of-plane kinematics. By the same token, that experiment will not obtain nearly as statistically precise data in the kinematics which we plan to explore, especially at the higher internal momenta. The uncertainty in the R_{LT} response will be especially large, given that it must be determined from a difference of two cross sections, each of which will have relatively large statistical errors. The Hall B experiment is complementary to this proposal in that it involves detection of protons moving in the backward direction relative to \vec{q} . It, therefore, primarily involves detection of a spectator proton with the neutron being the struck particle.

4 Kinematic Definitions and Formalism

The kinematics for $(e, e'p)$ are shown in Figure 2. The incident electron energy is e , the scattered electron energy is e' , the ejectile (*i.e.* proton) momentum is p and the angle between the proton and the momentum transfer, \vec{q} , is θ_{pq} . The azimuthal angle between the electron scattering plane and the hadronic plane (containing \vec{q} , \vec{p} and the momentum of the recoiling nucleus, \vec{p}_r (the recoiling nucleus is a neutron in the case of ${}^2\text{H}(e, e'p)n$)) is ϕ_x . For protons in the scattering plane and forward of \vec{q} (*i.e.* between \vec{q} and the incident electron direction), $\phi_x = 0^\circ$ and for protons backward of \vec{q} , $\phi_x = 180^\circ$. One can also define θ_{cm} which is the proton angle relative to \vec{q} in the rest frame of the final hadronic system. In this proposal, protons emitted backward of \vec{q} ($\phi_x = 180^\circ$) are assigned a negative value of θ_{cm} . Other kinematic quantities referred to in this proposal are: θ_e (the electron scattering angle), θ_p (the proton angle relative to the beam), ω (the energy transfer), $Q^2 = |\vec{q}|^2 - \omega^2$ (the square of the four-momentum transfer), x (the Bjorken x variable; $x = Q^2/(2m\omega)$ with m the proton mass) and y (related to the component of the initial proton momentum along \vec{q}). Finally, the initial proton momentum, \vec{p}_i , is equal to $-\vec{p}_r$ in Plane Wave Impulse Approximation (PWIA), but is not an observable quantity.

In the One Photon Exchange Approximation (OPEA), the unpolarized cross section for ${}^2\text{H}(e, e'p)n$ can be expressed in terms of four response functions [3], each of which

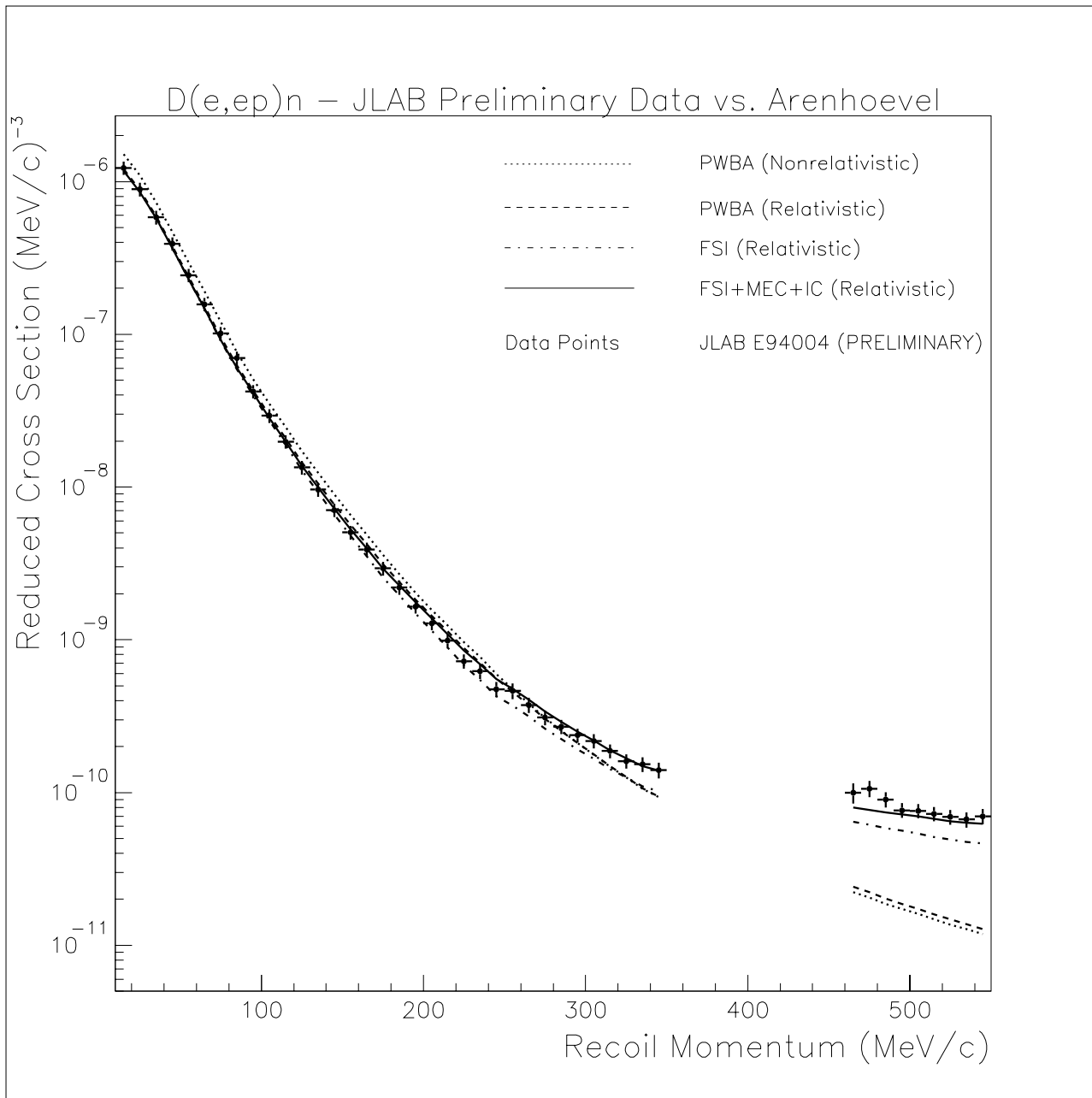


Figure 1: ${}^2\text{H}(e, e'p)n$ preliminary data from JLAB Hall A Experiment E94-004. The data include a 10% systematic error which is expected to be reduced to 5% in the final analysis. The various curves are from H. Arenhövel after acceptance averaging. The gap in the spectrum is due to a physical obstruction which obscured the proton spectrometer's view of the target for a certain range of angles. Unfortunately, this obstruction could not be removed during this short, preliminary run.

reflects different bilinear products of various components of the nuclear current :

$$\frac{d^4\sigma}{d\omega d\Omega_e dT_p d\Omega_p} = \frac{m|\vec{p}|}{16\pi^3} \sigma_M [v_L R_L + v_T R_T + v_{LT} R_{LT} \cos \phi_x + v_{TT} R_{TT} \cos 2\phi_x].$$

The more general case, including beam and recoil polarization has been worked out in detail [4]. For the current case of a specific final state (*i.e.* fixed missing mass), the response functions depend on \vec{q} , ω , and θ_{pq} (or equivalently θ_{cm} or p_r). The v 's are known kinematic factors weighting the various virtual photon polarization states and σ_M is the Mott cross section. By varying the kinematics so as to keep the response functions fixed, each may be separately determined. This proposal involves separating R_{LT} which is accomplished by selecting two kinematics, one with protons forward and the other with protons backward of \vec{q} . This changes the $\cos \phi_x$ factor multiplying R_{LT} from +1 to -1, respectively so that the difference of cross sections gives, to within an overall factor, R_{LT} . Since R_{LT} can be separated at fixed electron kinematics, it is technically less challenging than separating R_L and R_T .

5 Physics Motivation

5.1 Importance of the Deuteron

The deuteron, as the only bound two-nucleon system represents the simplest manifestation of the nuclear force. It therefore provides a benchmark in nuclear physics for one cannot hope to understand complex nuclei without first understanding the deuteron.

Although the deuteron is a loosely bound system its high momentum structure is strikingly similar to that of more complex nuclei [5]. Thus, measurement of high momentum components of the deuteron wave function can guide our understanding of the correlation structure of complex nuclei. Beyond about 0.3 GeV/c recoil momentum, the D-state component of the wave function is emphasized. A precise measurement in this range would provide important constraints for nucleon-nucleon potentials. It should be stressed, however, that the momentum distribution is not an observable and can only be extracted in the context of a model. For example, final state interactions can significantly alter the momentum of the detected nucleon and therefore the inferred initial momentum. Studies of the deuteron will also help to pin down these effects (see below) so that more quantitative statements about the deuteron wave function can be made. This information is important input for the understanding of the structure of more complex nuclei.

An example is the recently approved Hall A proposal to measure the $^{16}\text{O}(e, e'p)$ reaction [6] which is an update of an earlier Hall A measurement. The most modern relativistic Distorted Wave Impulse Approximation (DWIA) calculations were quite successful in reproducing the p -shell data from this earlier experiment and also showed evidence of dynamical relativistic effects in the left-right asymmetry (related to R_{LT}) [7]. The new ^{16}O proposal plans to push the kinematics to higher recoil momenta to test whether or where the single-particle DWIA model breaks down. Our $^2\text{H}(e, e'p)n$ proposal also involves measurements of R_{LT} (and hence the left-right asymmetry) over a range of Q^2 and p_r to test the validity of various relativistic treatments. As the deuteron is a simpler system, it provides a natural starting point for testing such models. The information gleaned from our experiment will be a critical component to interpreting this other experiment.

Coincidence ${}^2\text{H}(e, e'p)n$ reactions are particularly well suited to NN interaction studies. Below pion threshold, the final state is completely specified. For example, Fabian and Arenhövel have performed a nonrelativistic treatment of deuteron electrodisintegration in $(e, e'p)$ in which they examined the importance of interaction effects (Meson Exchange Currents (MEC) and Isobar Configurations (IC)) over the kinematical phase space below pion threshold [8]. Off the quasielastic peak they predict large changes in the cross section (reflecting mostly the transverse response, R_T) due to the presence of these interaction effects. In particular, at low momentum transfers and high np relative energies, they expect large modifications from ICs. Conversely, at high momentum transfers and low np relative energies, they expect large modifications from MECs. Therefore, by performing systematic studies over a broad kinematical range, the role played by various interaction effects can be quantified. Further, at large values of Q^2 , relativistic effects should be important. In fact, data at relatively low Q^2 from NIKHEF already indicate the need for a relativistic treatment in order to properly describe the R_{LT} response function [9] [10].

The deuteron is a valuable tool not only for what it can tell us about the nuclear force but also as a source of neutrons. Lacking pure neutron targets, the deuteron with its relatively loose binding is often chosen for studies of the structure of the neutron. Measurements of elastic electron scattering from deuterium have been used extensively in order to extract the long sought after and poorly known neutron electric form factor, G_{En} . There is also considerable interest in ${}^2\text{H}(\vec{e}, e'\vec{n})p$ polarization transfer measurements since various calculations predict that at small recoil momentum the observable of interest is sensitive to G_{En} [11] but relatively insensitive to NN interaction effects and to the deuteron wavefunction [12]. All of the above neutron studies rely on the assumption that nuclear corrections for the deuteron are either small or well understood. It is therefore vitally important to these measurements that this assumption be thoroughly tested. Understanding the deuteron is also important for measurements employing deuterium targets to determine the spin structure function of the neutron.

Finally, by studying the very short distance structure of the deuteron, one may determine whether or to what extent the description of nuclei in terms of nucleon/meson degrees of freedom must be supplemented by inclusion of explicit quark effects. This issue is of fundamental importance to nuclear physics.

5.2 Overview of Existing Data on ${}^2\text{H}(e, e'p)n$

The large body of data on the ${}^2\text{H}(e, e'p)n$ reaction serves as further testament to the importance of this reaction in nuclear physics. However, only with JLAB's unique combination of energy, current, duty factor and control of systematics (achievable in Hall A) can a truly systematic study be undertaken. This is especially true if one wishes to understand the short-distance structure of the deuteron where one needs both high energies and high luminosity/duty factor.

The short range structure of the deuteron is best revealed by measuring very high recoil momenta in ${}^2\text{H}(e, e'p)n$. Further, separations of the cross section into the various response functions allow one to exploit the sensitivity inherent in various interferences of components of the nuclear current. There is a substantial body of data on this reaction, including unseparated cross sections [13, 14, 15, 16] as well as separations of the various response functions [9, 17, 18, 19, 20, 21, 22, 23, 24]. Further, several experiments involving measurement of the ejected proton polarization have been carried out at Bates [25, 26, 27].

For the cross section measurements, limitations in energy of the various facilities (Bates/Saclay/NIKHEF/Mainz) have frustrated attempts to access the short distance structure of the deuteron [14, 16]. This limitation necessarily forces measurement of very high recoil momenta to energy transfers far above the quasielastic peak. Thus, for the Turck-Chieze and high recoil Blomqvist data, the kinematics were in the delta-region where lack of knowledge of the reaction mechanism make it difficult to deduce aspects of the deuteron structure. Although this limitation is not shared by SLAC, limitations in current and duty factor restrict the range of recoil momenta there as well. Although the Mainz [16] measurement sampled recoils up to 928 MeV/c, the kinematics actually imply that the bulk of the cross section arises from interaction with the neutron, leaving the detected proton as a spectator. Within this proton spectator picture, the actual internal momentum probed in this process is not the recoil momentum, but the momentum of the detected proton (~ 670 MeV/c). Further, since the kinematics were in the delta-region of the inclusive (e, e') spectrum, the inclusion of virtual nucleon excitations was required to obtain agreement with the data. In contrast, at JLAB one can examine large recoil momenta at or even below quasifree kinematics, making the extraction of the deuteron structure less model-dependent. It is stressed that **JLAB is the only facility in the world where such a study can be undertaken**. This experiment would exploit this unique opportunity.

The $d(e, e')n$ separation experiments have revealed gaps in our understanding. Various calculations have difficulty reproducing both R_L and R_T [18, 20, 22]. The R_{LT} response and related A_ϕ asymmetry indicate the need for relativistic treatments [9, 19, 20, 21] but problems still exist in reproducing the data. Again, JLAB provides the kinematic flexibility to perform these separations over a broad range of recoil momenta and momentum transfers. Here, we focus on a separation of R_{LT} as it is less technically demanding than separations of R_L and R_T .

5.3 Motivation for Parallel/Anti-Parallel Kinematics

In order to unravel the deuteron short-distance structure, one must either select kinematics which minimize reaction effects or correctly account for such effects. One of the main obstructions is FSI (see Figure 1). FSI can change the cross section at high recoil momenta by an order of magnitude or more. These large effects result from strength at low initial proton momentum, p_i , appearing at higher inferred p_i due to np rescattering in the final state. Such effects are likely to be large in perpendicular kinematics, but can be substantially reduced in parallel/anti-parallel kinematics. A simple picture illustrates this and is shown in Figure 3. Here, it's assumed that the rescattering mostly results in a change of the proton angle and not its energy. In this case, rescattering can lead to a larger inferred initial momentum for perpendicular kinematics, whereas for parallel or anti-parallel kinematics, rescattering can only produce a smaller initial momentum. Thus, within this highly oversimplified picture, for the parallel and anti-parallel cases one does not get feeding from smaller initial momentum, in contrast to the case for perpendicular kinematics. Naturally, one needs to go beyond this and perform a real calculation. The results of Arenhövel's calculation are shown in Table 1 for the middle Q^2 kinematics of this proposal. Here, "FSI/PWBA" refers to his calculation including FSI effects compared to the one without (Plane Wave Born Approximation). It is seen that rescattering gives an enhancement factor of 14 for the highest recoil momentum measured, compared to only 2.5 for the anti-parallel kinematics case. **The conclusion: the high recoil momentum**

p_r	FSI/PWBA	FSI/PWBA
MeV/c	\perp Kin	Anti- \parallel Kin
160	0.7	0.9
270	1.2	0.9
440	8.0	1.4
600	14	2.5

Table 1: Comparison of effects of FSI for perpendicular kinematics vs. anti-parallel kinematics for the middle Q^2 kinematics. The column labeled “FSI/PWBA” is the ratio of Arenhövel’s calculation including FSI to his PWBA calculation. The comparison is made for $\phi_x = 0^\circ$ in perpendicular kinematics and for $x > 1$ in anti-parallel kinematics. The ratios are given for roughly comparable recoil momenta (first column) for the two measurements.

spectrum in parallel/anti-parallel kinematics is much more connected to the deuteron short-distance structure than in perpendicular kinematics.

For the “anti-parallel” kinematics measurements (*i.e.* the ones below the quasifree peak), the momentum transfer was chosen to be sufficiently large in order to avoid significant contribution of the “spectator diagram” where the neutron is struck and the spectator proton is detected. Figure 4 illustrates this. In the left panel, the proton, initially moving opposite to \vec{q} absorbs the momentum transfer leading to the final state shown (the neutron, as a spectator, simply keeps the momentum it had initially). The right panel shows the situation where the neutron receives \vec{q} and the proton is a spectator. For the situation shown, the proton spectator diagram corresponds to low proton initial momentum, \vec{p}_i , but high recoil momentum, \vec{p}_r (\vec{p}_r is just the neutron final state momentum). High \vec{p}_r does not, therefore, necessarily correspond to high internal (*i.e.* initial) proton momentum, and, in fact, the proton spectator diagram would dominate the cross section in this case. However, if one selects a momentum transfer more than twice the largest recoil momentum, this situation cannot arise since the proton spectator diagram will involve an initial momentum larger than that for the neutron spectator diagram. Thus, for our anti-parallel kinematics, we have chosen a momentum transfer which is more than twice as large as the highest recoil momentum sampled. The anti-parallel kinematics then corresponds to the virtual photon essentially reversing the direction of the struck proton (see Figure 5). The point at which the proton’s initial momentum is equal to $\vec{q}/2$ would then correspond to a final state where the neutron and proton are moving in the same direction with equal momentum. This corresponds to threshold electro-disintegration. To avoid this kinematics and the relatively large FSI which would result, \vec{q} had to be chosen somewhat above twice the highest sampled recoil momentum.

Due to the lower bound on Q^2 from the above arguments and due to the fact that at even higher Q^2 , calculations of FSI, *etc.* become more unreliable and counting rates become more problematic, the measurements in parallel/anti-parallel kinematics will focus on the middle Q^2 value. They will span values of x above and below the quasifree peak for fixed beam energy and electron scattering angle. Although FSI are expected to be

relatively smaller for parallel/anti-parallel kinematics, one must still account for these and other reaction effects. The precision of the data gathered here would be adequate to clearly quantify the importance of these effects. This is illustrated in Figures 6 and 7 which show calculations of the cross section by Arenhövel [28] for a sample of the kinematics which would be measured. (The labeling of the various panels corresponds with the kinematics tables given below. “PY_4” and “PY_2” correspond to $+y$, *i.e.* energy transfers above the quasifree peak. “q2_00” is for $y = 0$ (*i.e.* on top of the quasifree peak or at $x = 1$; this point is the same as the zero recoil momentum point of the middle Q^2 perpendicular kinematics measurement). Finally “NY_2” and “NY_4” correspond to $-y$, *i.e.* energy transfers below the quasifree peak.)

5.4 Motivation for Perpendicular Kinematics

Here, the focus would be on extraction of the R_{LT} response function. This response is expected to be sensitive to relativistic effects. Although covariant calculations have been performed for elastic ${}^2\text{H}(e, e')$ [29] and for ${}^2\text{H}(e, e'p)n$ [30], they always involve some simplifying assumptions. It is necessary to test these assumptions.

Recent calculations of Jeschonnek, Donnelly and Van Orden [31, 32] suggest that the bulk of the relativistic effects may be in the nucleon current operator, as opposed to the nuclear dynamics. They obtained good agreement between a manifestly covariant calculation involving the Gross equation [29] and a calculation using a nonrelativistic wave function and a relativistic nucleon current operator. In contrast, a calculation with a nonrelativistic wave function and current operator drastically failed to reproduce the results of the covariant calculation. This highlights the importance of doing a proper relativistic treatment. Further, if, indeed, the relativistic effects are mostly in the current operator, they can be incorporated for heavier nuclei using the same approach. Due to its more tractable nature, the deuteron provides a testing ground for such an approach.

The PWBA model of refs. [31, 32] has been applied to the kinematics of this proposal and results for the highest and lowest Q^2 kinematics are shown in Figures 8, 9, 10 and 11. In addition, for the middle Q^2 kinematics, the Jeschonnek *et al.* calculations are compared to calculations of Arenhövel [28] in Figures 12, 13 and 14. The main conclusions to draw from this large mass of curves are:

- The differences between the non-relativistic and relativistic calculations for R_{LT} are extremely large, even at the lowest Q^2 . Both the Jeschonnek and the Arenhövel calculations show this.
- The differences between the relativistic Arenhövel and Jeschonnek calculations are significant. This is seen in Figure 13.
- The D-state becomes very important for the higher values of θ_{cm} . Thus, the R_{LT} can provide constraints on the D-state and hence the NN tensor force.

6 Kinematics

The kinematics for the low, middle and high Q^2 R_{LT} measurements in perpendicular kinematics are given in Tables 2, 3 and 4 respectively. The coincidence rates for proton

Kinematics	Q^2 (GeV/c) ²	$ \vec{q} $ GeV/c	x	θ_{cm} deg	p_r GeV/c	e' GeV	p GeV/c	θ_p deg
q1_00	0.688	0.908	0.991	0	0	3.630	0.908	-59.87
q1_b1	0.688	0.908	0.991	-20	0.145	3.630	0.892	-69.04
q1_b2	0.688	0.908	0.991	-40	0.288	3.630	0.845	-78.29
q1_b3	0.688	0.908	0.991	-60	0.426	3.630	0.770	-87.72
q1_b4	0.688	0.908	0.991	-80	0.556	3.630	0.672	-97.40
q1_f1	0.688	0.908	0.991	+20	0.145	3.630	0.892	-50.71
q1_f2	0.688	0.908	0.991	+40	0.288	3.630	0.845	-41.45
q1_f3	0.688	0.908	0.991	+60	0.426	3.630	0.770	-32.02

Table 2: Kinematics for the low Q^2 measurement. The beam energy is fixed at 4.0 GeV and the electron scattering angle is fixed at 12.50°. Measurements q1_b1–q1_b4 have proton angles backward of \vec{q} and θ_{cm} is assigned a negative value in these cases. R_{LT} would be extracted using q1_b1–q1_b3 and q1_f1–q1_f3.

spectrometer settings forward of \vec{q} are typically significantly smaller than for settings backward of \vec{q} . This mainly stems from the asymmetrical way in which the \vec{q} vector is populated (the Mott cross section decreases with increasing scattering angle which implies that the event population favors \vec{q} backward of its central value). Therefore, for the two lower Q^2 settings, an asymmetric range of proton settings about \vec{q} results. Only the overlapping range of $|\theta_{cm}|$ will be used to extract R_{LT} .

Table 3 also lists the kinematics of the parallel/anti-parallel kinematics measurements, which includes an overlapping point with the middle Q^2 perpendicular kinematic measurement (“q2_00”). Only the cross sections will be measured in parallel/anti-parallel kinematics with no separations of the response functions.

7 Experimental Equipment

This experiment would use the standard Hall A setup, including the high resolution spectrometer pair. The 6 msr collimators would be used for both spectrometers. The standard detection systems including scintillator stack, VDCs and Particle ID counters (Aerogel Čerenkov in the proton arm and gas Čerenkov + shower counter in the electron arm) would be needed. The PID requirements of this experiment are quite modest.

Targets include the 15 cm liquid deuterium cryogenic target, the 15 cm liquid hydrogen target for calibration of the cross section and for kinematic definition and a thin carbon foil for spectrometer pointing studies.

Unpolarized beam of 100 μA maximum current is needed along with the standard beam rastering and monitoring equipment. The entire experiment would run at a fixed beam energy of 4 GeV.

Kinematics	Q^2 (GeV/c) ²	$ \vec{q}' $ GeV/c	x	θ_{cm} deg	p_r GeV/c	e' GeV	p GeV/c	θ_p deg
PY_4	1.185	2.246	0.321	0	0.409	2.035	2.655	-19.84
PY_3	1.333	2.065	0.415	0	0.345	2.888	2.410	-24.54
PY_2	1.481	1.899	0.541	0	0.264	2.542	2.163	-30.09
PY_1	1.628	1.755	0.721	0	0.155	2.796	1.910	-36.64
q2_00	1.776	1.637	0.995	0	0	3.049	1.637	-44.24
q2_b1	1.776	1.637	0.995	-10	0.117	3.049	1.629	-48.32
q2_b2	1.776	1.637	0.995	-20	0.234	3.049	1.604	-52.42
q2_b3	1.776	1.637	0.995	-30	0.351	3.049	1.564	-56.56
q2_b4	1.776	1.637	0.995	-40	0.470	3.049	1.508	-60.77
q2_b5	1.776	1.637	0.995	-50	0.589	3.049	1.439	-65.06
q2_f1	1.776	1.637	0.995	+10	0.117	3.049	1.629	-40.16
q2_f2	1.776	1.637	0.995	+20	0.234	3.049	1.604	-36.05
q2_f3	1.776	1.637	0.995	+30	0.351	3.049	1.564	-31.91
q2_f4	1.776	1.637	0.995	+40	0.470	3.049	1.508	-27.70
NY_1	1.827	1.604	1.128	0	0.072	3.137	1.532	-47.12
NY_2	1.879	1.575	1.292	0	0.160	3.225	1.415	-50.11
NY_3	1.930	1.550	1.497	0	0.274	3.313	1.276	-53.21
NY_4	1.981	1.530	1.763	0	0.443	3.401	1.087	-56.39

Table 3: Kinematics for the middle Q^2 measurement. The beam energy is fixed at 4.0 GeV and the electron scattering angle is fixed at 22.00°. Measurements q2_b1–q2_b5 have proton angles backward of \vec{q}' and θ_{cm} is assigned a negative value in these cases. Measurements PY_1–PY_4 are for positive y ($x < 1$) and measurements NY_1–NY_4 are for negative y ($x > 1$). R_{LT} would be extracted using q2_b1–q2_b4 and q2_f1–q2_f4.

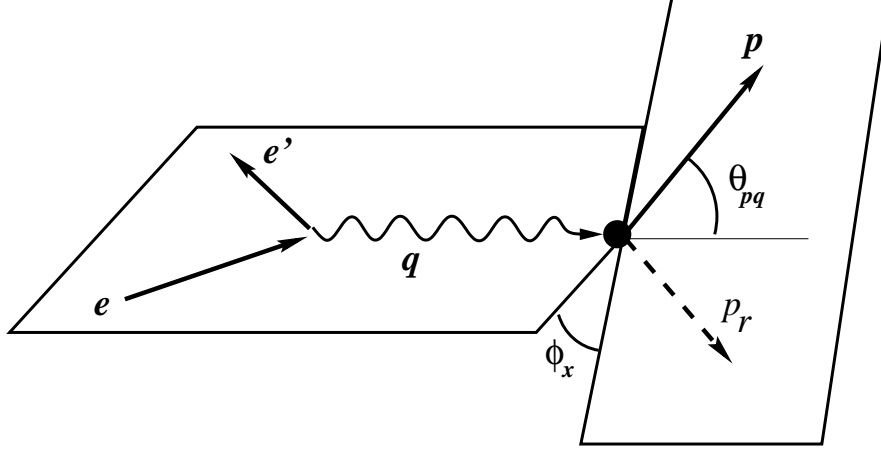


Figure 2: Kinematics for $(e, e'p)$. See the text for details.

Kinematics	Q^2 (GeV/c) ²	$ \vec{q} $ GeV/c	x	θ_{cm} deg	p_r GeV/c	e' GeV	p GeV/c	θ_p deg
q3_00	3.262	2.511	0.996	0	0	2.255	2.511	-31.00
q3_b1	3.262	2.511	0.996	-10	0.158	2.255	2.497	-34.61
q3_b2	3.262	2.511	0.996	-20	0.319	2.255	2.455	-38.24
q3_b3	3.262	2.511	0.996	-25	0.400	2.255	2.424	-40.08
q3_f1	3.262	2.511	0.996	+10	0.158	2.255	2.497	-27.39
q3_f2	3.262	2.511	0.996	+20	0.319	2.255	2.455	-23.76
q3_f3	3.262	2.511	0.996	+25	0.400	2.255	2.424	-21.92

Table 4: Kinematics for the high Q^2 measurement. The beam energy is fixed at 4.0 GeV and the electron scattering angle is fixed at 35.00°. Measurements q3_b1–q3_b3 have proton angles backward of \vec{q} and θ_{cm} is assigned a negative value in these cases. R_{LT} would be extracted using q3_b1–q3_b3 and q3_f1–q3_f3.

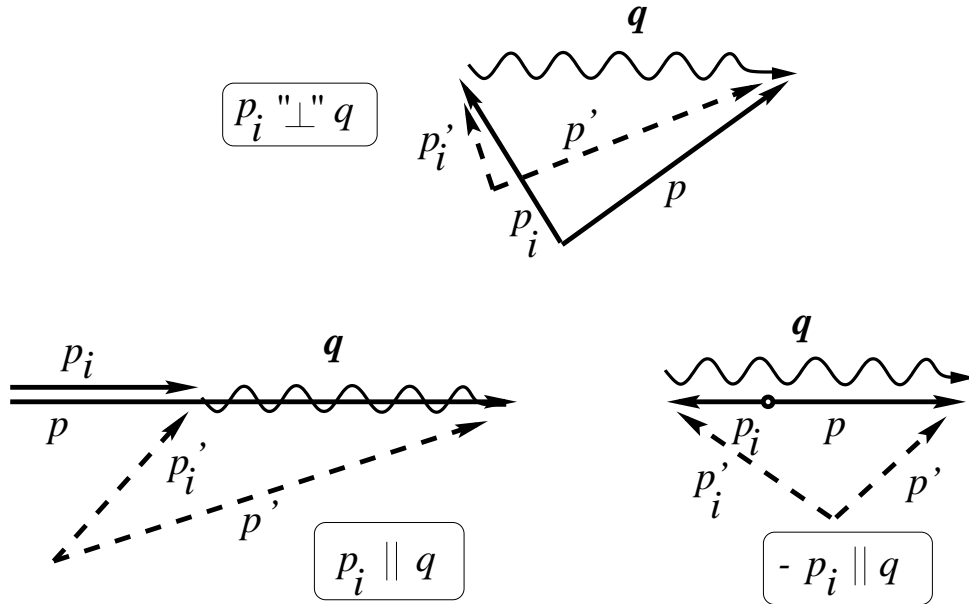


Figure 3: Rescattering cartoons. The measured values of the proton momentum (p) and momentum transfer (q) are shown by the solid arrows. The inferred value of the proton initial momentum is then p_i . However, the measured value of p can arise from a “true” value, p' (dashed arrow) which then changes to p by rescattering. The actual value of the initial momentum is then p'_i (dashed arrow). The situation is shown for “perpendicular”, parallel and anti-parallel kinematics. (Perpendicular kinematics refers to the case where the initial momentum and \vec{q} are roughly at right angles. More precisely, it corresponds to fixed \vec{q} and ω .) The perpendicular kinematic case is shown only for the undesirable situation where low initial momentum feeds high recoil momentum (the reverse is also possible).

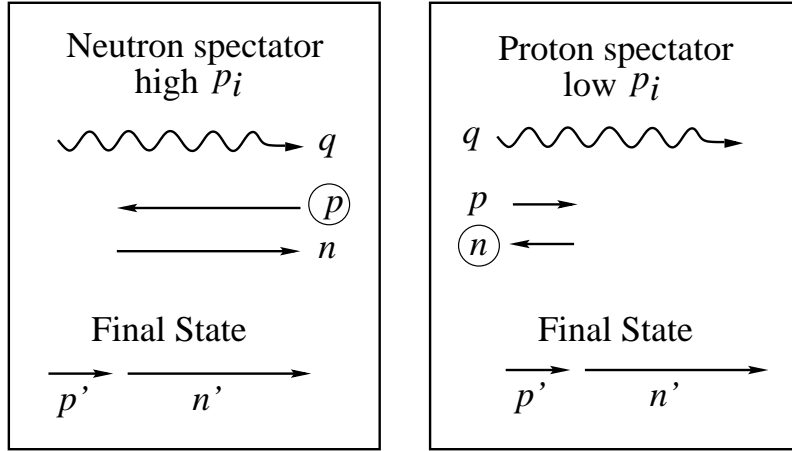


Figure 4: The proton and neutron are labeled p and n respectively. The struck particle in each case is circled. The final state momenta are indicated with primes. The left panel shows the situation when the proton is struck and the neutron is the spectator and vice versa for the right panel. Both situations lead to the same final state and are therefore experimentally indistinguishable. This illustrates that the proton spectator diagram, which corresponds to low initial momentum, can feed high p_r .

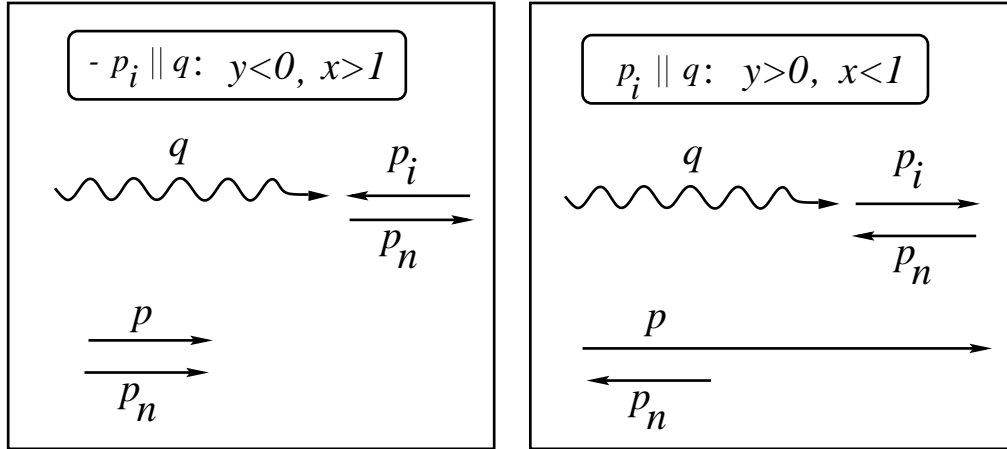


Figure 5: The left panel shows anti-parallel kinematics and the right shows parallel kinematics. In both cases it's assumed that the proton is struck so that $\vec{p}_i + \vec{q} = \vec{p}$. For illustrative purposes the left panel shows the situation for threshold breakup where the proton and neutron move off together with equal momenta. In this case, where $|\vec{q}| = 2|\vec{p}_i|$, the virtual photon effectively reverses the proton momentum leading to a small energy transfer (compared with the right panel).

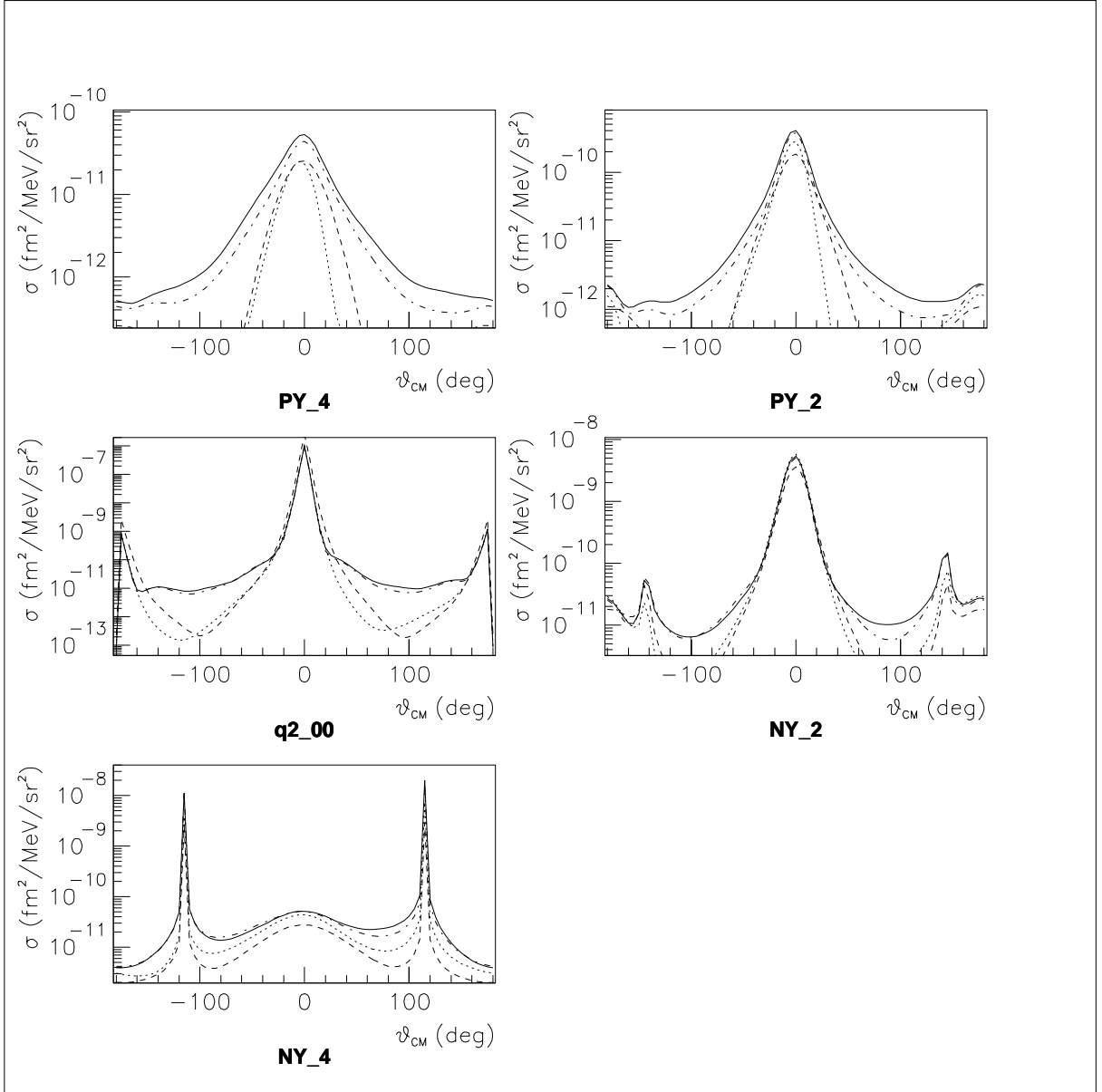


Figure 6: Calculations of the cross section for ${}^2\text{H}(e, e'p)n$ by Arenhövel for a sample of the parallel/anti-parallel kinematics measurements (see the text for explanation of the labels of each panel). The dashed curve is PWBA, the dotted curve includes relativistic corrections, the dot-dashed curve includes also FSI and the solid curve is the full result which includes also MEC and IC. Reading from left to right and then down the page, the energy transfer monotonically decreases. The sharp structures on the wings of the spectra result from singularities in the proton CoM to Lab solid angle Jacobian.

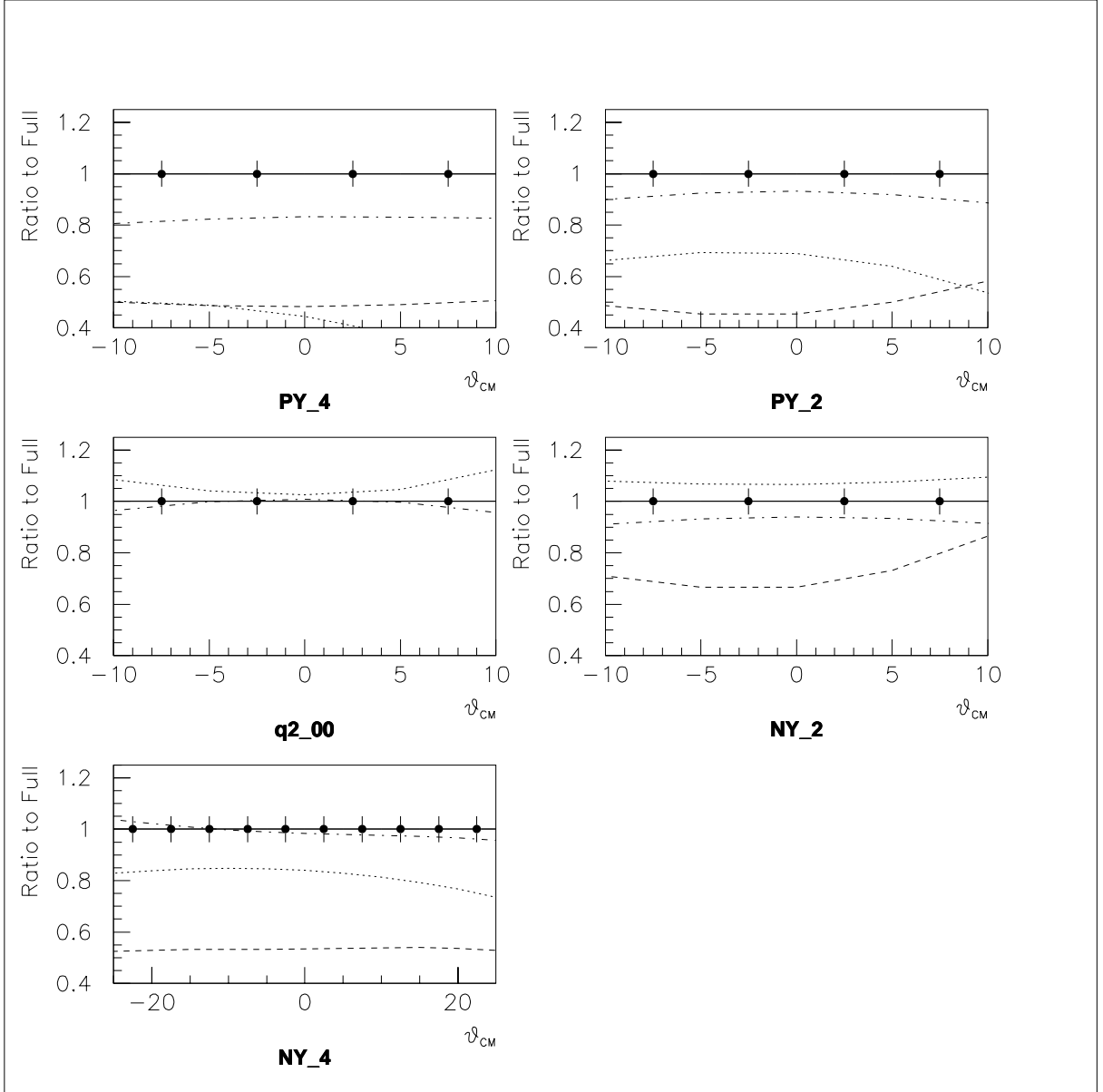


Figure 7: The ratio of each of Arenhövel's curves shown in Figure 6 to the full result. The labeling of the curves is the same as in Figure 6. The projected data are shown with 5% uncertainties per bin, which is an estimate of the systematic error. The statistical uncertainties per bin are smaller than this 5% and are, in most cases, negligible in comparison.

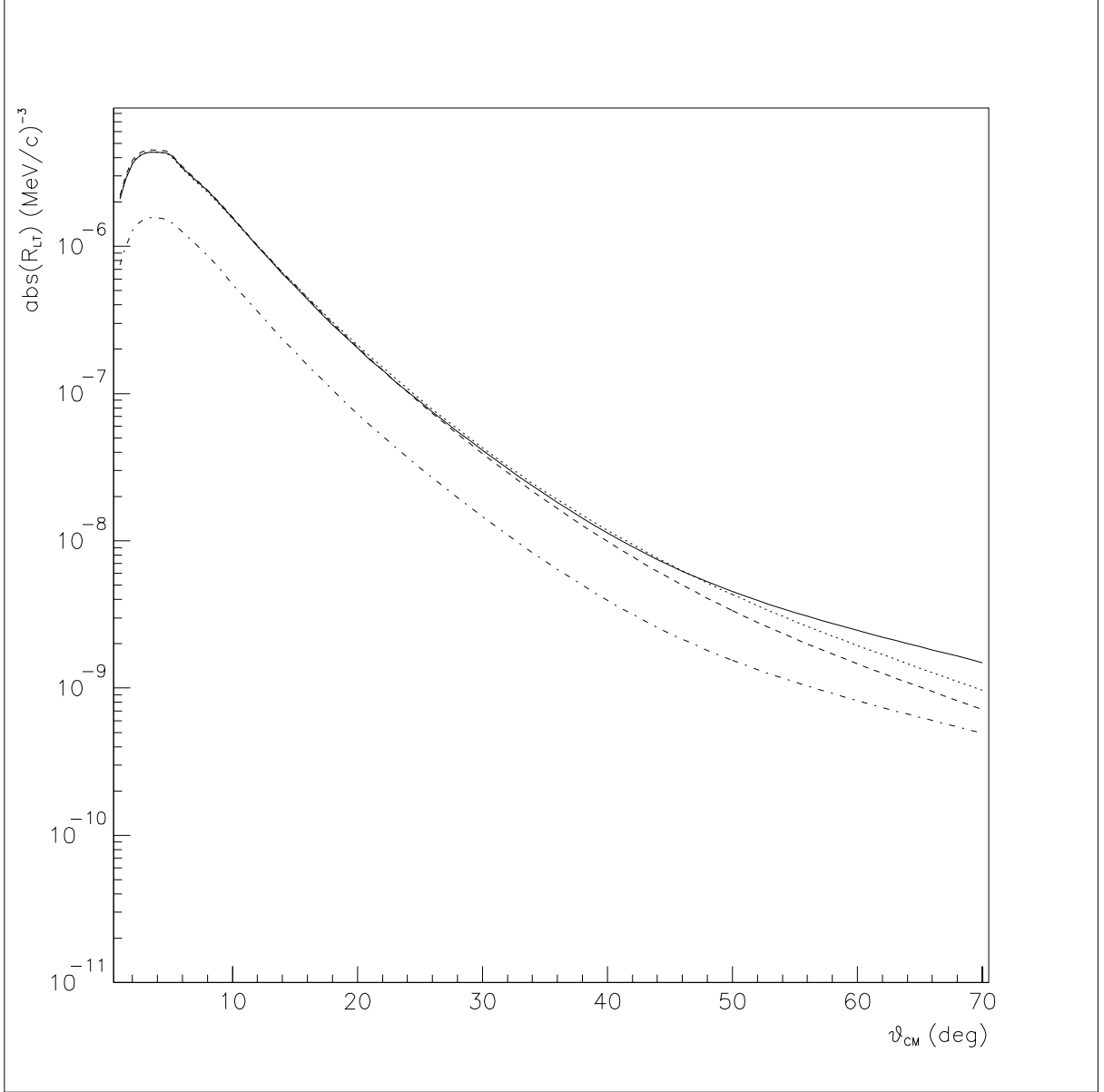


Figure 8: Calculations based on the PWBA code of Jeschonnek *et al.* for $|R_{LT}|$ for the lowest Q^2 measurement of this proposal. The solid line is for the Argonne V18 wavefunction, the dashed line is for the Bonn wavefunction, the dotted line is for the CD-Bonn wavefunction, and the dot-dashed line is for the non-relativistic calculation.

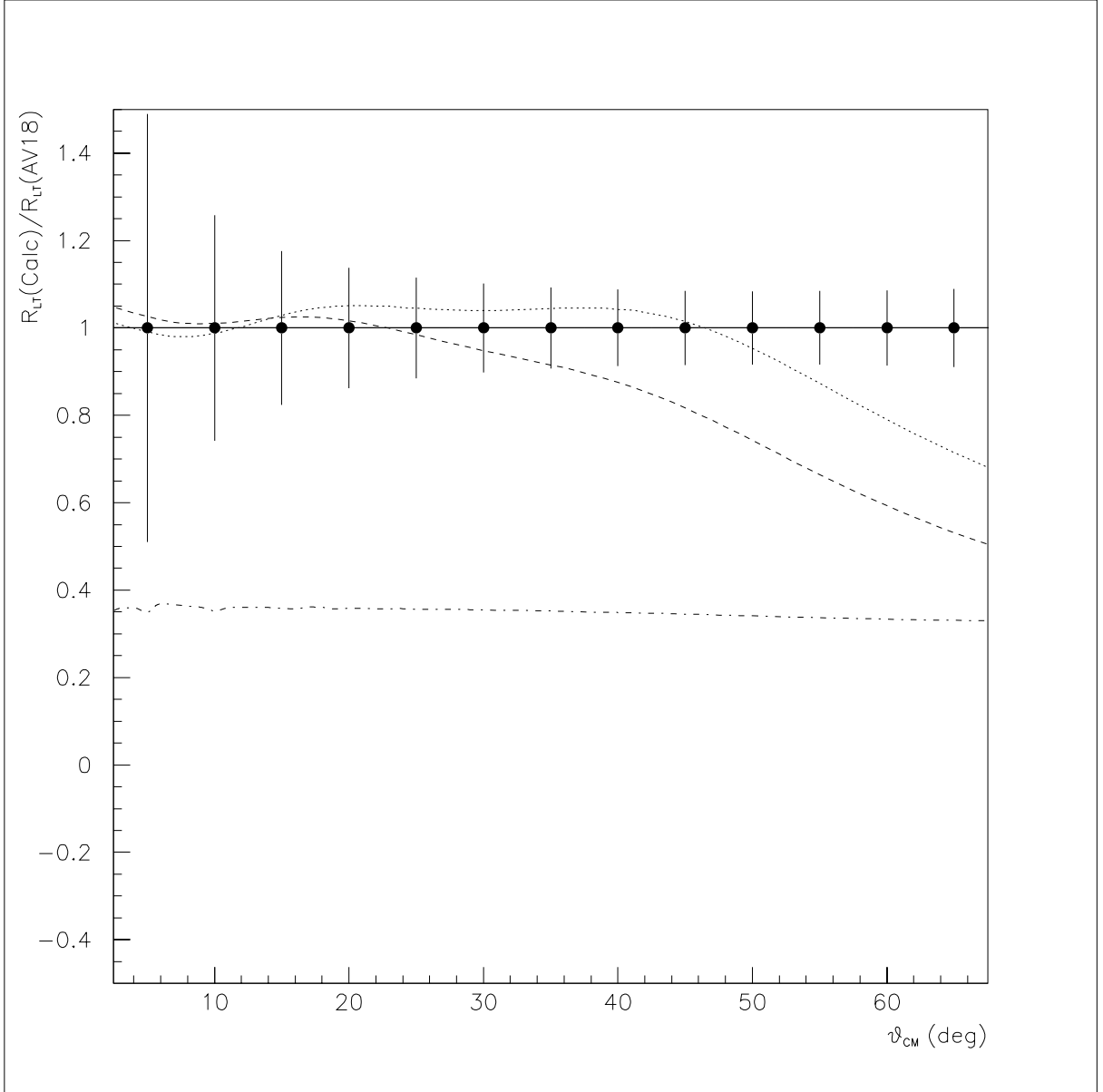


Figure 9: The ratio of each of the curves of Figure 8 (lowest Q^2 setting) to the Argonne V18 result. The curves labels are the same as for Figure 8. The projected data for this proposal are shown with 5% uncertainties in the cross sections which is an estimate of the overall systematic error. The statistical errors per bin are smaller than this 5% and, in most cases, negligible in comparison.

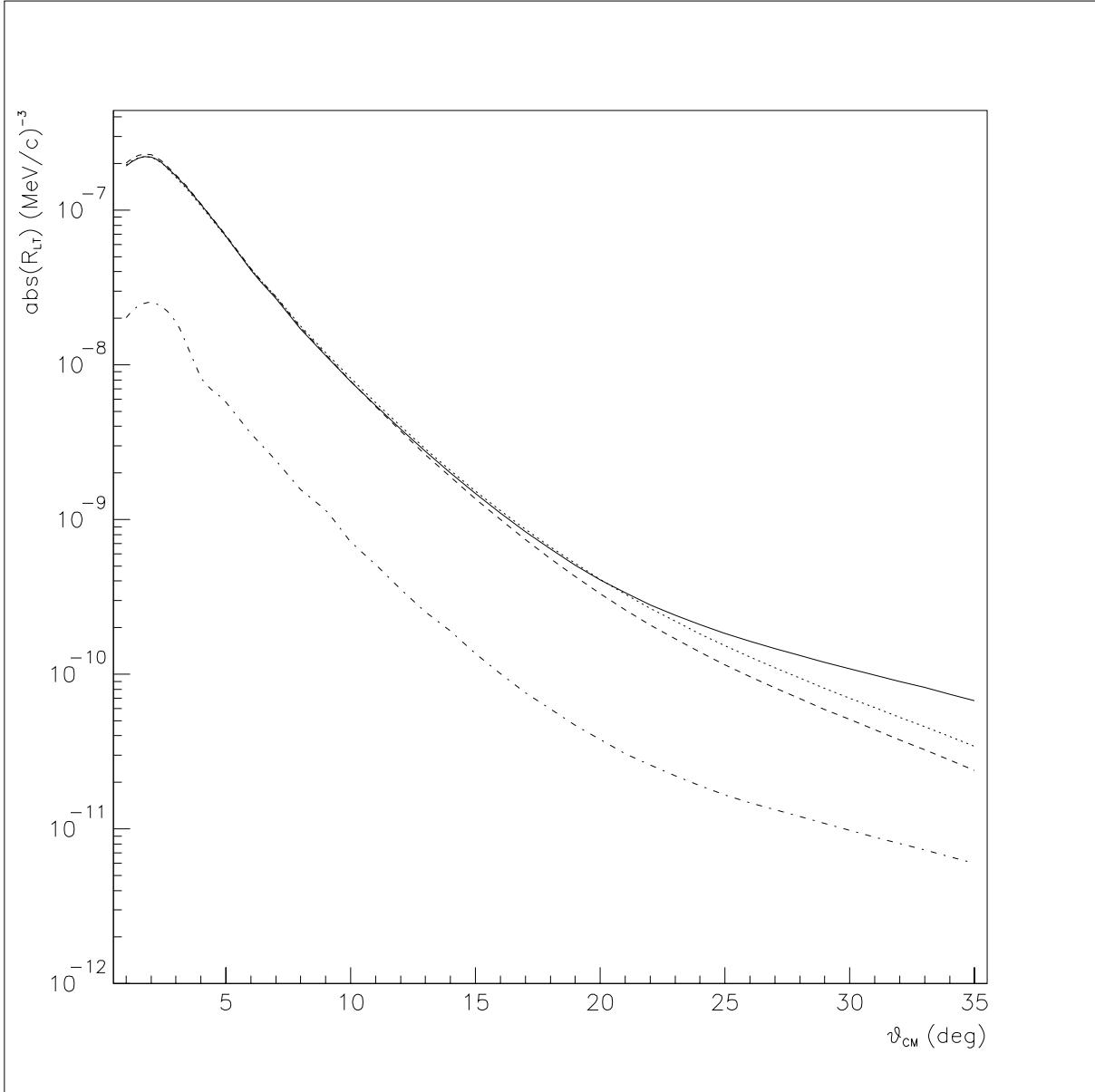


Figure 10: Same as Figure 8 except for the highest Q^2 kinematics.

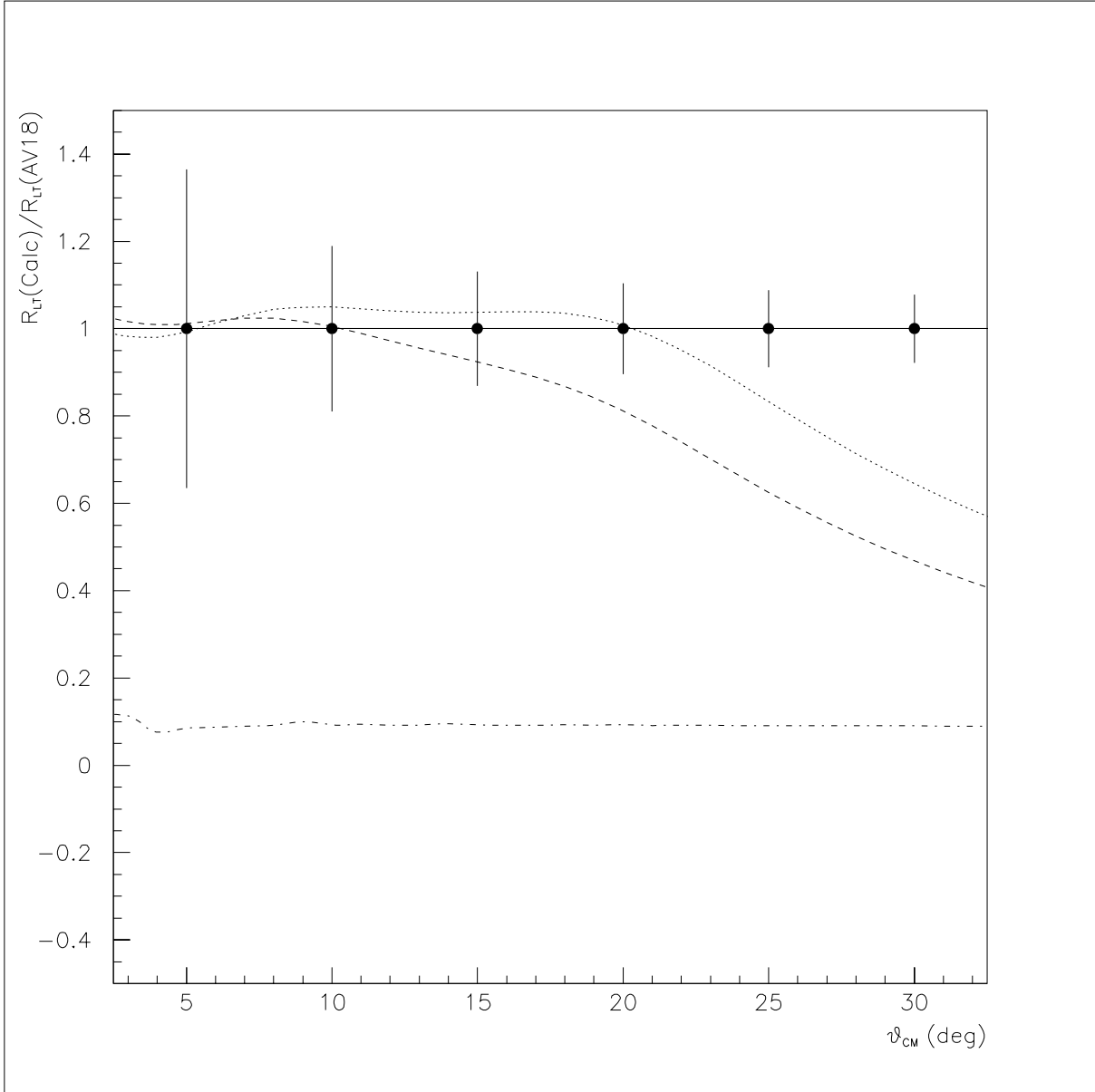


Figure 11: Same as Figure 9 except for the highest Q^2 kinematics.

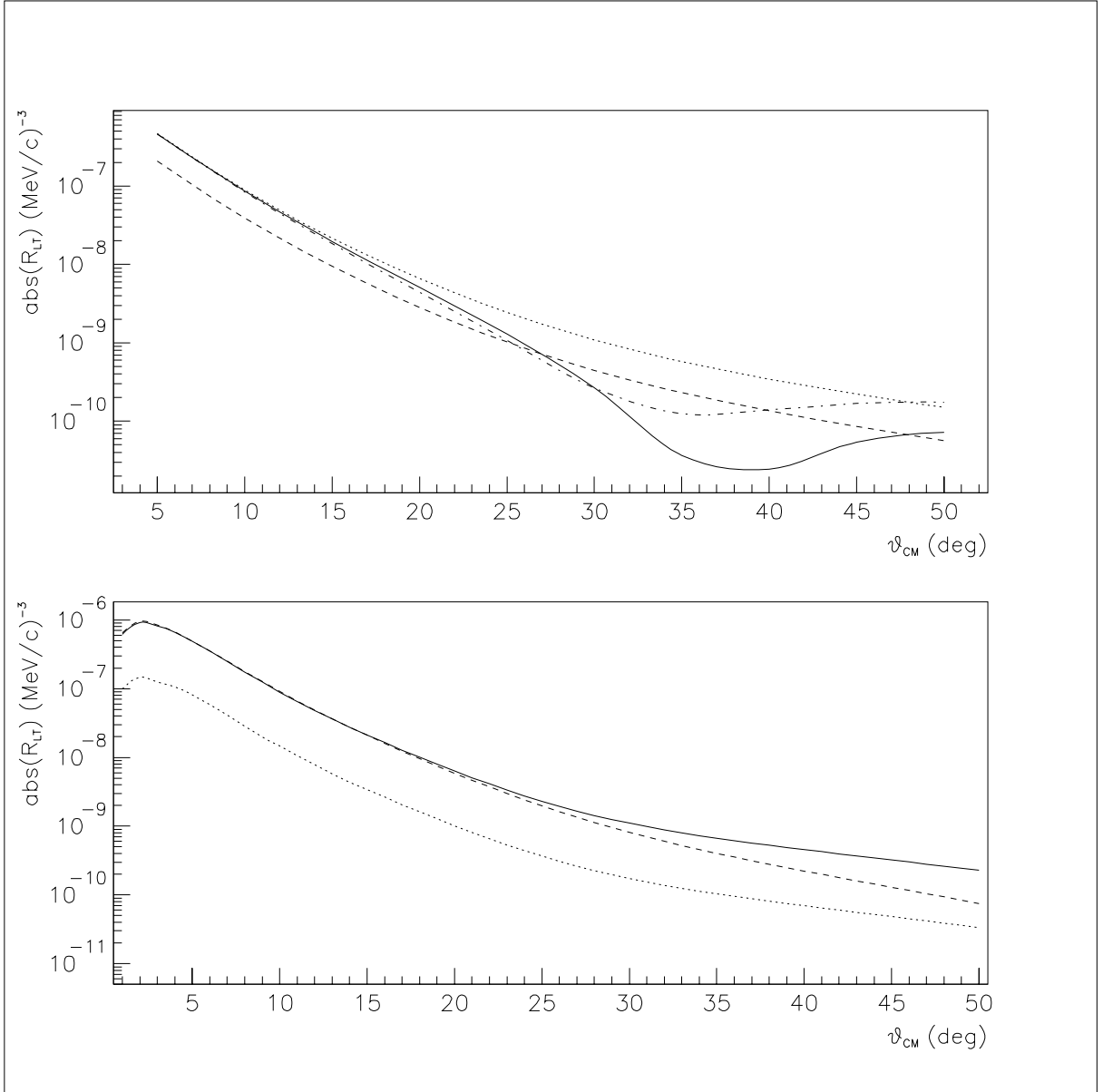


Figure 12: Upper panel: Calculations of Arenhövel for the middle Q^2 kinematics. The dashed curve is PWBA, the dotted curve includes relativistic corrections, the dot-dashed curve includes also FSI and the solid curve is the full result which includes also MEC and IC. Lower panel: Calculations based on the PWBA code of Jeschonnek *et al.* The solid curve uses the Argonne V18 wavefunction, the dashed curve uses the Bonn wavefunction, and the dotted curve is the non-relativistic result.

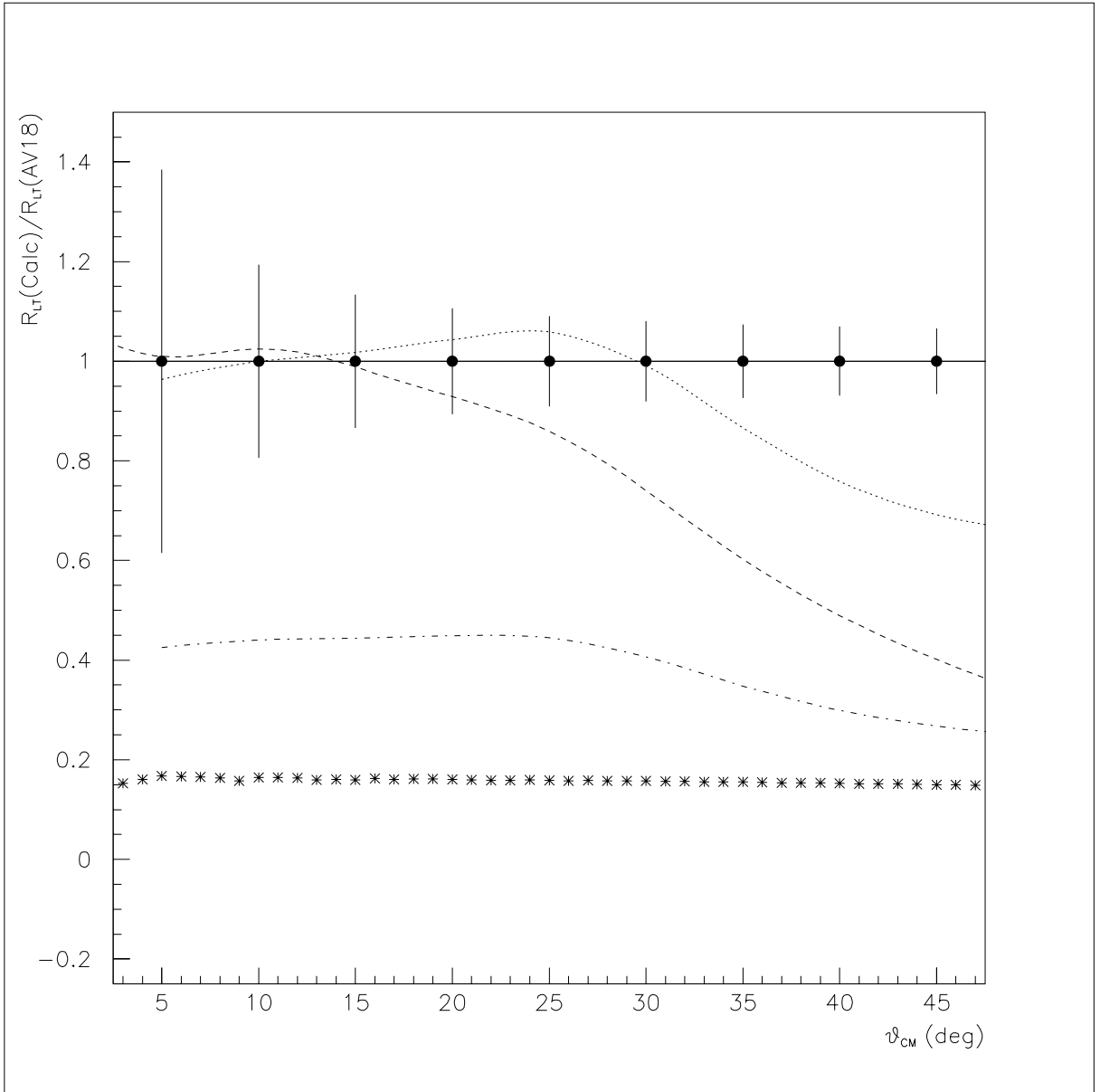


Figure 13: Calculation of Arenhövel and calculations based on the PWBA code of Jeschonnek *et al.* for the middle Q^2 kinematics. The solid curve is the Jeschonnek result using the Argonne V18 wavefunction, the dashed curve uses the Bonn wavefunction, the asterisks are the non-relativistic result, the dotted curve is the result of Arenhövel's PWBA calculation with relativistic corrections using the Bonn wavefunction and the dot-dashed curve is Arenhövel's non-relativistic result. The curves have each been normalized to the Argonne V18 curve. The projected data are shown with an overall 5% error per bin in the cross sections.

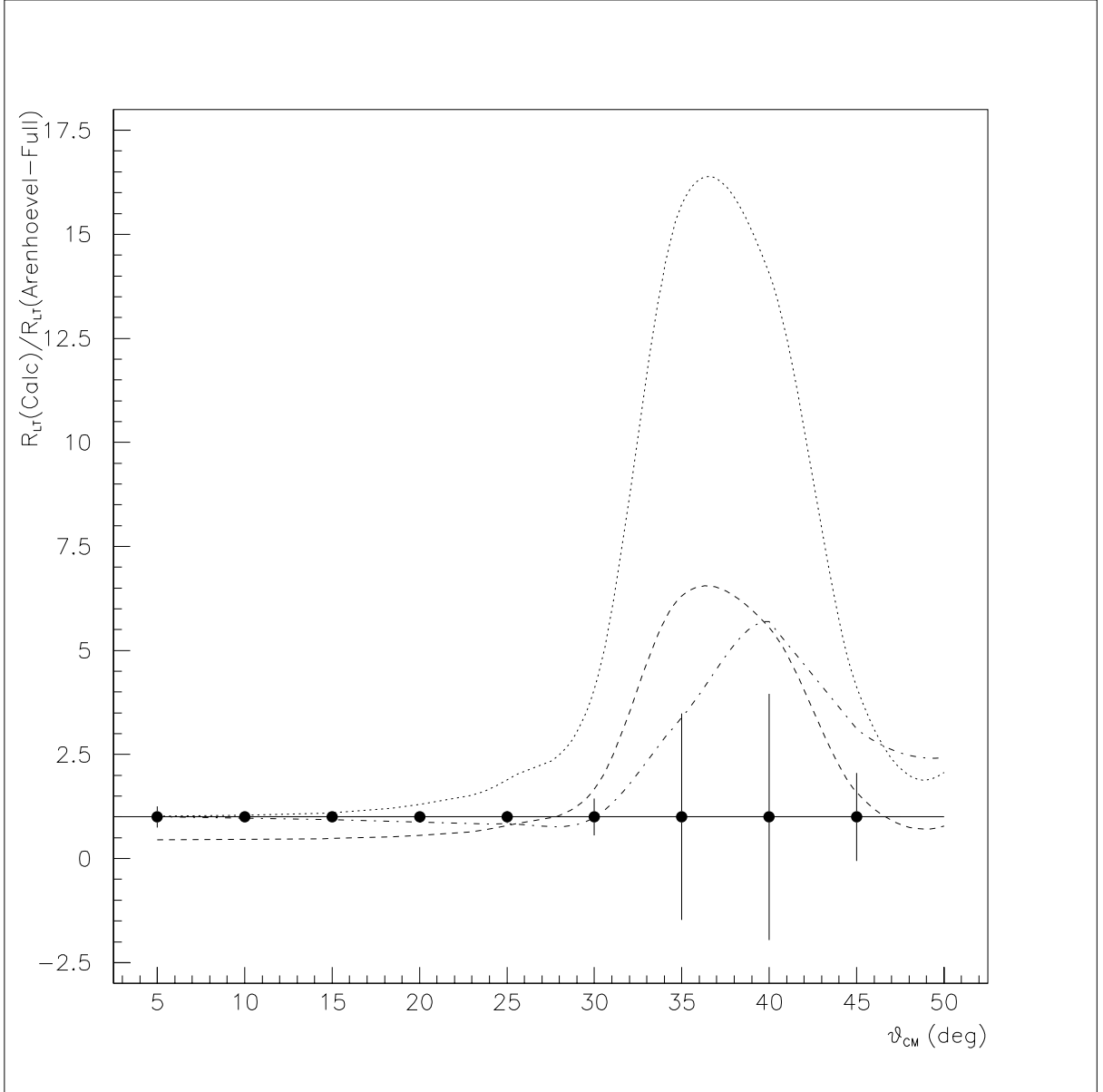


Figure 14: Calculations of Arenhövel for the middle Q^2 kinematics. The dashed curve is the PWBA calculation and the dotted curve includes relativistic corrections. The dot-dashed curve includes also FSI and the solid line is the full result including also MEC and IC. Each curve has been normalized to the full result. The projected data are shown with an overall 5% error per bin in the cross sections.

Kinematics	Beam Current μA	(e, e') KHz	(e, π^-) KHz	(e, p) KHz	(e, π^+) KHz
q1_00	15	115	4	11	7
q1_b1	60	427	14	2	23
q1_b2	60	410	14	1	18
q1_b3	60	397	13	1	9
q1_b4	60	403	13	2	8
q1_f1	30	258	9	71	16
q1_f2	20	193	7	72	13
q1_f3	10	113	4	54	8

Table 5: Singles rates for the low Q^2 measurement.

8 Single-Arm Rates

Single-arm background rates for (e, e') were calculated with the computer code QFSV and for (e, p) , (e, π^+) and (e, π^-) with the electro-production code EPC, both of Lightbody and O'Connell [33]. These codes were embedded in the $(e, e'p)$ Monte Carlo code, MCEEP [34], allowing the single-arm cross sections to be folded with the acceptance of the respective spectrometer. The results are shown in Tables 5, 6 and 7. The beam current was selected to keep the single-arm rates below 500 KHz per arm. The rates are not atypical of Hall A experiments and should pose no problems.

9 Coincidence Rates

The coincidence rates were calculated with the $(e, e'p)$ Monte Carlo code, MCEEP [34] using the PWBA model of Jeschonnek and the Argonne V18 wave function radiatively folded within MCEEP. This code has been used extensively to model experiments and compare data to folded theoretical calculations. The rates are given in Tables 8, 9 and 10.

Details of the various table entries follow:

- **DAQ Rate:** This is the total data acquisition rate which includes real coincidences and accidental coincidences within an 80 ns timing gate. The accidentals rates are based on products of the singles rates in each arm and include contributions from (e, e') and (e, π^-) in the electron arm and from (e, p) and (e, π^+) in the proton arm.
- **Coin Rate:** This is the real coincidence rate including radiative effects. The radiative tail was cut on missing mass ($\epsilon_m < 10$ MeV; about 8 MeV above the breakup threshold). This cut is necessary, since, otherwise, radiative effects can cause substantial feeding from low recoil momentum to high, heavily biasing the spectrum.

Kinematics	Beam Current	(e, e')	(e, π^-)	(e, p)	(e, π^+)
	μA	KHz	KHz	KHz	KHz
PY_4	60	27	54	241	56
PY_3	60	29	52	223	52
PY_2	70	26	58	233	54
PY_1	80	18	60	224	55
q2_00	100	14	28	101	58
q2_b1	100	13	27	1	27
q2_b2	100	12	25	1	1
q2_b3	100	12	24	1	<1
q2_b4	100	11	23	1	<1
q2_b5	100	11	22	1	<1
q2_f1	100	15	30	266	64
q2_f2	100	15	32	311	70
q2_f3	100	16	33	353	74
q2_f4	35	6	12	140	28
NY_1	100	10	11	46	54
NY_2	100	5	2	18	51
NY_3	100	1	<1	11	48
NY_4	100	<1	<1	36	45

Table 6: Singles rates for the middle Q^2 measurement.

Kinematics	Beam Current	(e, e')	(e, π^-)	(e, p)	(e, π^+)
	μA	KHz	KHz	KHz	KHz
q3_00	100	<1	27	113	21
q3_b1	100	<1	27	1	<1
q3_b2	100	<1	25	<1	<1
q3_b3	100	<1	25	<1	<1
q3_f1	100	<1	29	297	69
q3_f2	100	<1	29	330	77
q3_f3	100	<1	30	345	79

Table 7: Singles rates for the high Q^2 measurement.

Kinematics	Beam Curr.	DAQ Rate	Coin Rate	S:N	Time	Err
	μA	KHz	Hz		hours	%
q1_00	15	0.18E+01	0.16E+04	0.13E+05	0.98E-02	2.0
q1_b1	60	0.11E+01	0.28E+03	0.33E+04	0.55E-01	2.0
q1_b2	60	0.68E+00	0.19E+02	0.31E+03	0.78E+00	2.0
q1_b3	60	0.35E+00	0.47E+01	0.65E+02	0.31E+01	2.0
q1_b4	60	0.34E+00	0.18E+01	0.19E+02	0.81E+01	2.0
q1_f1	30	0.20E+01	0.12E+03	0.69E+02	0.14E+00	2.0
q1_f2	20	0.14E+01	0.28E+01	0.25E+01	0.76E+01	2.0
q1_f3	10	0.58E+00	0.24E+00	0.54E+00	0.27E+02	5.0
Total					47	

Table 8: Coincidence rates for the low Q^2 measurement. Times correspond to the given statistical uncertainties per 20 MeV/c bin in p_r .

Kinematics	Beam Curr. μA	DAQ Rate KHz	Coin Rate Hz	S:N	Time hours	Err %
PY_4	60	0.19E+01	0.30E+00	0.67E+00	0.21E+02	5.0
PY_3	60	0.18E+01	0.68E+00	0.14E+01	0.18E+02	3.0
PY_2	70	0.19E+01	0.29E+01	0.64E+01	0.64E+01	2.0
PY_1	80	0.18E+01	0.41E+02	0.13E+03	0.39E+00	2.0
q2_00	100	0.15E+01	0.93E+03	0.71E+04	0.17E-01	2.0
q2_b1	100	0.25E+00	0.16E+03	0.16E+06	0.86E-01	2.0
q2_b2	100	0.14E-01	0.98E+01	0.11E+05	0.14E+01	2.0
q2_b3	100	0.33E-02	0.15E+01	0.19E+04	0.40E+01	3.0
q2_b4	100	0.21E-02	0.52E+00	0.71E+03	0.42E+01	5.0
q2_b5	100	0.17E-02	0.24E+00	0.35E+03	0.91E+01	5.0
q2_f1	100	0.13E+01	0.12E+03	0.35E+03	0.13E+00	2.0
q2_f2	100	0.14E+01	0.44E+01	0.11E+02	0.38E+01	2.0
q2_f3	100	0.17E+01	0.39E+00	0.89E+00	0.38E+02	3.0
q2_f4	35	0.24E+00	0.31E-01	0.51E+00	0.52E+02	10.0
NY_1	100	0.71E+00	0.54E+03	0.10E+05	0.27E-01	2.0
NY_2	100	0.11E+00	0.71E+02	0.60E+04	0.19E+00	2.0
NY_3	100	0.72E-02	0.30E+01	0.14E+04	0.45E+01	2.0
NY_4	100	0.38E-03	0.14E+00	0.67E+03	0.16E+02	5.0
Total					179	

Table 9: Coincidence rates for the middle Q^2 measurement. Times correspond to the given statistical uncertainties per 20 MeV/c bin in p_r .

Kinematics	Beam Curr.	DAQ Rate	Coin Rate	S:N	Time	Err
	μA	KHz	Hz		hours	%
q3_00	100	0.37E+00	0.72E+02	0.16E+05	0.20E+00	2.0
q3_b1	100	0.11E-01	0.97E+01	0.40E+06	0.14E+01	2.0
q3_b2	100	0.12E-02	0.22E+00	0.14E+05	0.96E+01	5.0
q3_b3	100	0.95E-03	0.69E-01	0.44E+04	0.31E+02	5.0
q3_f1	100	0.85E+00	0.66E+01	0.63E+03	0.22E+01	2.0
q3_f2	100	0.97E+00	0.96E-01	0.82E+01	0.28E+02	5.0
q3_f3	100	0.10E+01	0.24E-01	0.19E+01	0.77E+02	7.0
Total					150	

Table 10: Coincidence rates for the high Q^2 measurement. Times correspond to the given statistical uncertainties per 20 MeV/c bin in p_r .

- **S:N:** This is the signal-to-noise ratio (*i.e.* the real rate divided by the accidentals rate into a 5 ns timing window). Here, the accidentals rates include only (e, e') in the electron arm and (e, p) in the proton arm since particle ID will almost completely remove the other backgrounds. Further, it's assumed that accidentals are reduced by a factor of 5 from requiring a consistent vertex from both spectrometers and another factor of 10 from a missing mass cut.
- **Time:** The acquisition times are for the quoted statistical errors. They include computer deadtime of 10% per KHz data acquisition rate as well as an overall 30% inefficiency factor. This 30% inefficiency is based on experience from Experiment E94-004 and reflects anticipated acceptance cuts to eliminate the relatively poorly understood edges as well as VDC hit multiplicity cuts to deal with multiple track events (especially important at the higher singles rates). (The radiative losses have already been included in the coincidence rates.)
- **Err:** The statistical uncertainty per 20 MeV/c bin in p_r . Each measurement comprises roughly 15 of these bins. The statistical uncertainty includes contributions from the accidentals within the coincidence resolving time (assumed here to be 5 ns).

The beam times were optimized within the following constraints:

- $\text{S:N} \geq 0.5$
- $\text{DAQ Rate} \leq 2 \text{ KHz}$
- $\text{Single-arm Rates per arm} \leq 500 \text{ KHz}$
- $\text{Beam Current} \leq 100 \mu\text{A}$

Item	Beam hours
Acquisition - low Q^2	47
Acquisition - middle Q^2	179
Acquisition - high Q^2	150
$^1\text{H}(e, e'p)$ calibrations	3
Alignment $^1\text{H}(e, e'p)$ + sieve	12
Angle/field changes (32)	16
Pointing measurements	16
BCM calibrations	4
Arc+ep Energy Measurements	8
Harp scans	4
Target boiling curve	2
White spectrum scans	8
Total (hours)	449
Total (days)	19

Table 11: Beam time summary.

10 Systematic and Statistical Uncertainties

We estimate the overall systematic error in the cross sections to be roughly 5%. This estimate is based largely on experience from the October 1999 $^2\text{H}(e, e'p)n$ run and related calibration measurements. There, the predominant sources of uncertainty were found to be the determination of the spectrometer central angles [35] and calibration of the spectrometer solid angle. The former is important due to the strong kinematic variation of the $^2\text{H}(e, e'p)n$ cross section. Both of these uncertainties will be minimized by making calibration measurements with the liquid hydrogen target.

The statistical uncertainties per bin given in the rate tables are usually significantly less than 5%. This allows a precise determination of the shape of the cross section within a kinematic setting since the systematic error mainly results in an overall shift of the entire spectrum. Further, the relatively small statistical errors allow investigation of the systematics for a variety of cuts.

11 Beam Time Summary

The beam time summary is given in Table 11. The acquisition time is roughly 16 days and the overhead/calibration time is roughly 3 days for a total of 19 days.

12 Acknowledgment

One of the co-spokespersons (P.E. Ulmer) wishes to express his sincere thanks to H. Arenhövel for providing calculations for this proposal.

References

- [1] H. Arenhövel, private communication. See also: W. Leidemann, E.L. Tomusiak and H. Arenhövel, Phys. Rev. C **43**, 1022 (1991).
- [2] JLAB Hall B Experiment E94-102, *Electron Scattering from a High Momentum Nucleon in Deuterium*, K. Griffioen and S. Kuhn, co-spokespersons.
- [3] M. Gourdin, Nuovo Cim. **21**, 1094 (1961).
- [4] A. Picklesimer and J.W. Van Orden, Phys. Rev. C **35**, 266 (1987).
- [5] C. Marchand *et al.*, Phys. Rev. Lett. **60**, 1703 (1988).
- [6] JLAB Hall A Experiment E00-102, *Testing the Limits of the Single Particle Model in $^{16}\text{O}(e, e'p)$: An Update to E89-003*, W. Bertozzi, K. Fissum, A. Saha and L. Weinstein, co-spokespersons.
- [7] J. Gao *et al.*, Phys. Rev. Lett. **84**, 3265 (2000).
- [8] W. Fabian and H. Arenhövel, Nucl. Phys. **A314**, 253 (1979).
- [9] M. van der Schaar *et al.*, Phys. Rev. Lett. **68**, 776 (1992).
- [10] E. Hummel and J.A. Tjon, Phys. Rev. C **49**, 21 (1994).
- [11] R.G. Arnold, C.E. Carlson and F. Gross, Phys. Rev. C **23**, 363 (1981); H. Arenhövel, W. Leidemann and E.L. Tomusiak, Z. Phys. A **331**, 123 (1988).
- [12] H. Arenhövel, Phys. Lett. **B199**, 13 (1987) and private communication; A.Yu. Korchin, Yu.P. Mel'nik and A.V. Shebeko, Sov. J. Nucl. Phys. **48**, 243 (1988); M.P. Rekalov, G.I. Gakh and A.P. Rekalov, J. Phys. G. **15**, 1223 (1989).
- [13] M. Bernheim *et al.*, Nucl. Phys. **A365**, 349 (1981).
- [14] S. Turck-Chieze *et al.*, Phys. Lett. **142B**, 145 (1984).
- [15] H. Breuker *et al.*, Nucl. Phys. **A455**, 641 (1986).
- [16] K.I. Blomqvist *et al.*, Phys. Lett. B **424**, 33 (1998).
- [17] T. Tamae *et al.*, Phys. Rev. Lett. **59**, 2919 (1987).
- [18] M. van der Schaar *et al.*, Phys. Rev. Lett. **66**, 2855 (1991).
- [19] F. Frommberger *et al.*, Phys. Lett. B **339**, 17 (1994).
- [20] J.E. Ducret *et al.*, Phys. Rev. C **49**, 1783 (1994).
- [21] H.J. Bulten *et al.*, Phys. Rev. Lett. **74**, 4775 (1995).
- [22] D. Jordan *et al.*, Phys. Rev. Lett. **76**, 1579 (1996).

- [23] A. Pellegrino *et al.*, Phys. Rev. Lett. **78**, 4011 (1997).
- [24] W.-J. Kasdorp *et al.*, Phys. Lett. B **393**, 42 (1997).
- [25] B.D. Milbrath *et al.*, Phys. Rev. Lett. **80**, 452 (1998).
- [26] B.D. Barkhuff, Ph.D. thesis, MIT (1997).
- [27] K. Joo, Ph.D. thesis, MIT (1997).
- [28] H. Arenhövel, private communication (2000).
- [29] J.W. Van Orden, N. Devine and F. Gross, Phys. Rev. Lett. **75**, 4369 (1995).
- [30] E. Hummel and J.A. Tjon, Phys. Rev. C **49**, 21 (1994).
- [31] S. Jeschonnek and T.W. Donnelly, Phys. Rev. C **57**, 2438 (1998).
- [32] S. Jeschonnek and J.W. Van Orden, Phys. Rev. C **62**, 044613 (2000).
- [33] J.W. Lightbody and J.S. O'Connell, Computers in Physics, May/June 1988, p. 57.
- [34] P.E. Ulmer, computer program MCEEP, *Monte Carlo for (e, e'p) Experiments*, JLAB Technical Note # 91-101 (1991).
- [35] P.E. Ulmer, H. Ibrahim and N. Liyanage, *Calibration of Beam Energy and Spectrometer Central Angles using Hall A HRS in $^1\text{H}(e, e'p)$* , JLAB Technical Note # 00-024 (2000).